ARTICLE

Photon Momentum Enabled Light Absorption in Silicon

Sergey S. Kharintsev,* Aleksey I. Noskov, Elina I. Battalova, Liat Katrivas, Alexander B. Kotlyar, Jovany G. Merham, Eric O. Potma, Vartkess A. Apkarian, and Dmitry A. Fishman*

Read Online

ACCESS | Metrics & More | Article Recommendations | SI Supporting Information

ABSTRACT: Photons do not carry sufficient momentum to induce indirect optical transitions in semiconducting materials, such as silicon, necessitating the assistance of lattice phonons to conserve momentum. Compared to direct bandgap semiconductors, this renders silicon a less attractive material for a wide variety of optoelectronic applications. In this work, we introduce an alternative strategy to fulfill the momentum-matching requirement in indirect optical transitions. We demonstrate that when confined to scales below ∼3 nm, photons acquire sufficient momentum to allow electronic transitions at the band edge of Si without the assistance of a phonon. Confined photons allow simultaneous energy and momentum conservation in two-body photon-electron scattering; in effect, converting silicon into a direct bandgap semiconductor. We show that this less-explored concept of light-matter interaction leads to a marked increase in the absorptivity of Si from the UV to the near-IR. The strategy provides opportunities for more efficient use of indirect semiconductors in photovoltaics, energy conversion, light detection, and emission.

$$\sigma_k \sigma_r = \left(n + \frac{1}{2}\right)$$

KEYWORDS: *photon momentum, light-matter interaction, confined photon, diagonal transitions, semiconductors*
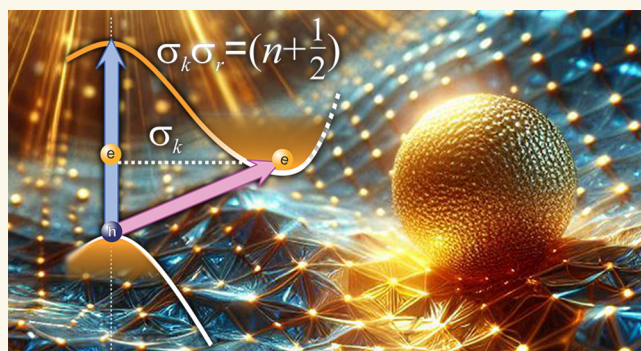
INTRODUCTION

Both energy and momentum must be conserved in light-matter interactions. This requirement dictates that the energy difference between the material states must match the photon energy. Because the photon momentum in free space is negligible in comparison to the momentum of electrons, satisfying the two conservation laws at the bandgap of semiconductors is conditional on the vertical alignment of the bottom of the conduction band and the top of the valence band. When aligned, the bandgap is classified as direct and the transition is optically allowed, depicted by vertical arrows in the material's energy band diagram. In case the states are offset in k-space, the bandgap is indirect. This scenario applies to the bandgap of silicon at 1.1 eV (at $\lambda_0 = 1130$ nm). As can be seen in the band structure provided in Figure 1a, the band extrema at the Γ and X points are separated by a lattice momentum of $k \sim 2\pi/a$, where $a = 0.54$ nm is the lattice constant, which is 3 orders of magnitude larger than the momentum $k_0 = 2\pi/\lambda_0$ of a free space photon. While direct optical transitions at this energy are forbidden, momentum conservation can be satisfied through indirect, phonon-assisted transitions. The three-body nature of electron-photon-phonon scattering in indirect transitions is responsible for the 2 orders of magnitude weaker

absorptivity of Si near its band edge, relative to direct bandgap semiconductors,[1,2] as illustrated in Figure 1c.

Despite silicon's preeminence in optoelectronics, its unfavorable optical properties impose fundamental limitations on its technological applications, as in solar energy conversion and photovoltaic industries, where Si strongly dominates.[3] Because of silicon's modest light absorption, over 90% of currently installed solar cells use crystalline silicon with a thickness of more than 100 μm to achieve efficient light-to-energy conversion throughout the visible and near-infrared range (Supplementary Part 1, Figure SF1). In contrast, in direct bandgap semiconductors, similar conversion efficiencies can be reached at thicknesses of 0.2 μm due to their greater absorptivity.[4] Since the price of conventional solar cells is intimately related to the cost of the semiconductor material, silicon's weak absorption coefficient lowers its practical
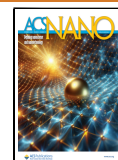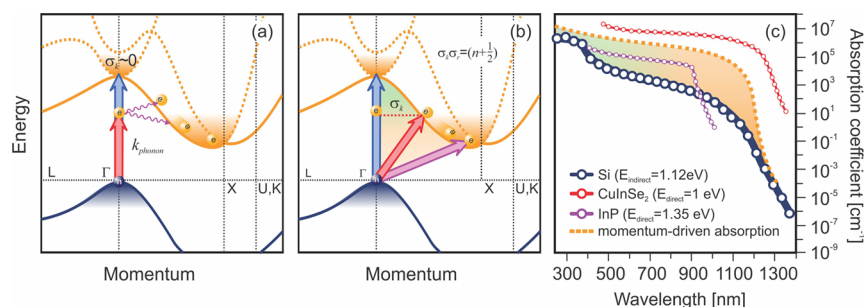
Figure 1. (a) Energy-momentum diagram for optical transitions in pure Si with free space photons. The arrows indicate direct (blue arrow, $\sigma_k \sim 0$) and indirect optical transitions (red and velvet arrows, $k_{phonon} > 0$). (b) Energy-momentum diagram showing optical transitions enabled by the momentum distribution σ_k of confined photons without the need of lattice phonons. Both diagrams (a) and (b) depict optical transitions near the Γ point, excluding other momentum-enabled transitions at various other points across the Brillouin zone. (c) Absorption spectrum of Si,[5] and direct bandgap semiconductors InP[6,7] and CuInSe$_2$.[8] Dashed curves and shaded regions indicate the increase of the absorption coefficient across a broad spectral range due to photon momentum-enabled transitions.

implementation as a competitive renewable energy resource,[9] and challenges its promise as a viable alternative to fossil fuels.[10]

This challenge has spurred numerous efforts to improve light management in silicon.[11] For instance, light trapping in black[12] or textured silicon[13] has been implemented to enhance absorption. Other efforts employ subwavelength structures, such as nanocones,[14] to trap photons by increasing the effective refractive index or the local density of optical states.[15] Such approaches include the use of plasmonics, typically in the form of metallic nanoparticles that act as near-field concentrators.[16] However, the performance of plasmonic structures has proven to be limited because of scattering and ohmic losses;[17] moreover, plasmonic resonances are typically narrow in comparison to the solar spectrum, no part of which can be spared.

The photon momentum can be boosted by 2−3 orders of magnitude to match the lattice momentum of Si by confining it on nanometric scales.[18,19] Photons can be most tightly confined in plasmonic cavities or junctions, where local fields are carved by the atomistic morphology of the structure.[20] Such picocavities[21−23] can reach effective volumes of $V_e < (1$ nm$)^3$, invariably at junctions that contain atomic protrusions.[24] Confinement of photons on atomic scale has been visualized with tip-enhanced Raman microscopy, characterized as a Gaussian light field with a lateral distribution of standard deviation $\sigma_r = 0.14$ nm (0.16 nm fwhm image resolution).[25,26] An increase in the momentum of localized excitation fields has previously been suggested as an explanation for the enhancement of the interband transition rate in metals, as observed in two-photon electron emission experiments on roughened Ag films.[27] A different, but related effort has pointed out that the increased momentum associated with surface polaritons can be leveraged to enable indirect transitions in a variety of materials,[28] and its application to indirect semiconductors has been insinuated.[29] For the case of bulk Si, it was modeled by Yamaguchi and Noda et al. to show that with a point-dipole acting as a point source placed within ~1 nm from the surface, the absorption spectrum is enhanced and extends to the band edge.[30,31] The effect has been suggested to explain the increased photosensitivity of silicon photodiodes decorated with metallic nanoparticles.[32] However, the most significant effect was observed with the largest ~100 nm gold spheres, a result that goes counter to the momentum expansion effect,

which inversely scales with particle size and is maximized at the atomistic scale.

To estimate the extent of the momentum distribution of a confined photon and its significance for facilitating optical transitions in silicon, we consider the light-induced dipolar polarization of a small particle of diameter d near the silicon interface. We can model this polarization as a singly occupied $(n = 1)$ electromagnetic mode with a spatial extent described by its standard deviation $\sigma_r \sim d/2.355$. The distribution of momenta can be obtained through the quantum uncertainty principle $\sigma_r\sigma_k = (n + 1/2)$, where n is the expectation value of the occupation number operator $\hat{N} = a^\dagger a$ (see Supporting Information Part 2). For example, for high photon energies (transitions closer to the direct bandgap of Si), the amount of confinement $\sigma_r \sim 0.35$ nm ($d \sim 0.85$ nm) and $\sigma_r \sim 0.4$ nm ($d \sim 1$ nm) is required to reach 633 nm/1.96 eV and 532 nm/2.33 eV points in the conduction band, respectively (red arrow, Figure 1b). To permit direct photon momentum-enabled transitions near the indirect bandgap (~1127 nm/1.1 eV, purple arrow Figure 1b), confinement of $\sigma_r \sim 0.16$ nm ($d \sim 0.38$ nm) is needed to cover the distance of $\sigma_k \sim 9.2$ nm^{-1} from the Γ point to the lowest energy near the X point.[33] Ultimately, for an atomically confined photon, $\sigma_r = 0.14$ nm, the standard deviation of its momentum distribution, $\sigma_k \sim 11$ nm^{-1}, spans the entire Brillouin zone of Si, $2\pi/a = 11.5$ nm^{-1}. In effect, all $k \leftrightarrow k'$ transitions become accessible with near unity probability through direct diagonal transitions.

In this work, we experimentally demonstrate that such an effect is indeed observed when light is confined on 1−3 nm asperities. We carry out measurements in three different experimental arrangements. In the first, as a proxy to absorption, we measure the heating of a silicon cantilever through Raman thermometry. We observe a dramatic increase in light absorption, which leads to melting of the silicon tip near ~1−2 nm structures and insignificant heating near >3 nm asperities, even though the latter structures sustain much larger plasmonic fields and thus a higher field enhancement. In a second configuration, we deposit nanometer-sized structures on a Si wafer and perform reflection measurements to demonstrate that it is the absorption that is enhanced across the full solar spectrum, down to silicon's band edge. In a final experiment, we show a significant increase in the photocurrent in a Si photodiode when its surface is decorated with nanometric asperities. While these observations cannot be explained through plasmonic enhancement effects, we show
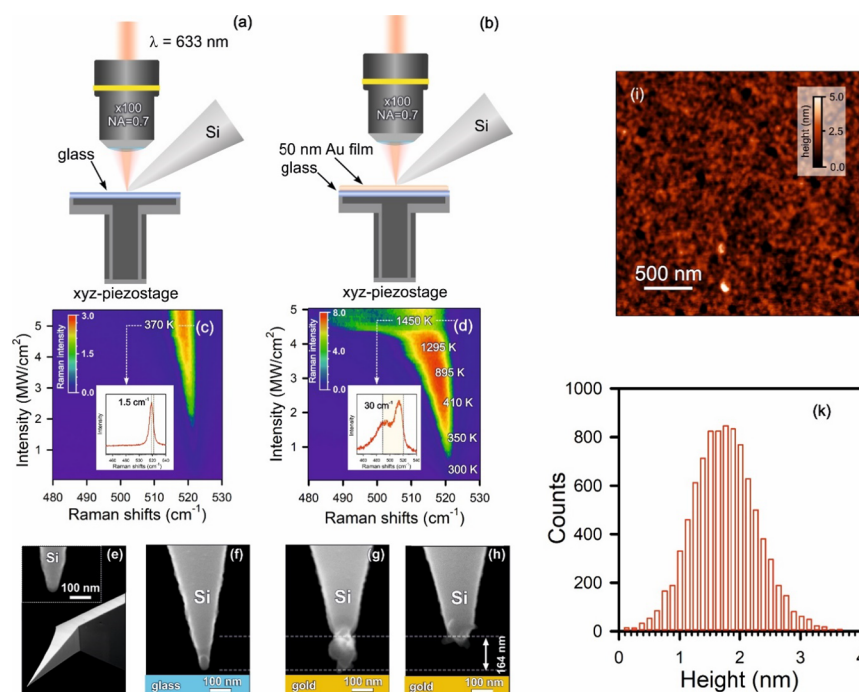
Figure 2. Experimental configuration when a Si AFM cantilever is placed over (a) bare glass and (b) a 50 nm gold film. Panels (c) and (d) show Si Raman spectra as a function of laser intensity for either bare glass or a smooth gold film. The insets indicate Raman spectra along the dashed straight line. (e−h) SEM images of an intact AFM cantilever with the tip apex before (inset) and after illumination for different substrates. (i) AFM image of the 50 nm thick Au film and its (k) surface roughness height distribution histogram centered at $h_0 = 1.7$ nm ($\sigma = 0.55$ nm).

that they follow the trends predicted by the confined photon momentum.

RESULTS AND DISCUSSION

The first set of measurements is carried out with a tip-enhanced Raman scattering (TERS) microscope, equipped with a Si AFM cantilever oscillating in semicontact mode over a planar substrate. The tip is illuminated with a focused, linearly polarized beam derived from a continuous laser at 633 nm (Figure 2a,b). We record the Raman response of crystalline Si at 521 cm^{-1}, and we monitor the evolution of the line intensity, spectral shift, and width. The calibrated temperature dependence of this Raman mode makes it possible to estimate the absolute lattice temperature (see Supporting Information, Part 3).[34,35] Figure 2c shows the evolution of the Si Raman spectrum as a function of the incident laser intensity as the tip is positioned over a bare glass substrate. We observe a small blueshift of the line as the laser intensity is increased, indicating heating. Under 5 MW/cm^2 irradiation levels, the line shifts by 1.5 cm^{-1} (inset of Figure 2c), corresponding to a temperature rise of $\Delta T \sim 70$ K above ambient temperature (see Supporting Information and Figure SF2). Although these temperatures are well below the melting point of Si, we confirm through postexperiment SEM images that the tip retains its structural integrity during these Raman measurements (Figure 2f).

We observe strikingly different behavior when the tip is placed over a 50 nm Au film, evaporated on a glass substrate (Figure 2b). The smooth gold surface is characterized by height variations, with a mean value of $h_0 = 1.7$ nm and a standard deviation of 0.55 nm (Figure 2f,k). At irradiation intensities above 4 MW/cm^2, the spectrum splits into two distinct components, corresponding to contributions from the hot apex at wavenumbers below 500 cm^{-1} and from the cold

shaft at 521 cm^{-1}, which both occupy the collection volume of the objective lens (inset of Figure 2d). At these laser intensities, we observe a 30 cm^{-1} line shift, indicating a tip temperature rise in excess of $\Delta T = 1180$ K (Figure 1d). As revealed through Raman imaging (see Supporting Information, Part 4), the "hot" part extends about ∼300 nm out from the apex (mapped at 480 cm^{-1}) into the Si material, whereas the colder part of the tip in the detection volume remains at ambient temperature (mapped at 521 cm^{-1}). The temperature near the apex exceeds the Si melting point (1683 K), conditions under which the tip melts and the apex pinches off, as verified by postexperiment SEM images (Figure 2g,h). In all tip-melting experiments, the pinch-off consistently happens 150−250 nm from the apex. In fact, as substantiated by the simulations, such melting behavior would only be expected if input fluxes were ∼25x higher than used in the current experiment (see Supporting Information Part 5 and Figure SF4).

The experiments suggest an enhanced optical absorption in silicon when the tip is placed over a gold surface with nanoscale surface roughness, while the effect is absent on bare glass. Enhanced absorption can be anticipated when the incident field is locally enhanced at Au structures. However, the measured surface roughness of $h_0 = 1.7 \pm 0.6$ nm (Figure 2k) is well below the spatial scale needed to support strong localized surface plasmon resonances.[36]

Heat dynamics in solids at the nanoscale can be rather complex, as diverse mechanisms can play a role (see Supporting Information Part 5).[37] To obtain reliable estimates of the tip temperature, we carried out FDTD/FEM simulations. The simulations show that, for a hemispherical Au protrusion of 2 nm, the penetration depth of the near-field into the Si tip apex is 2−3 nm (Figure SF4) and the
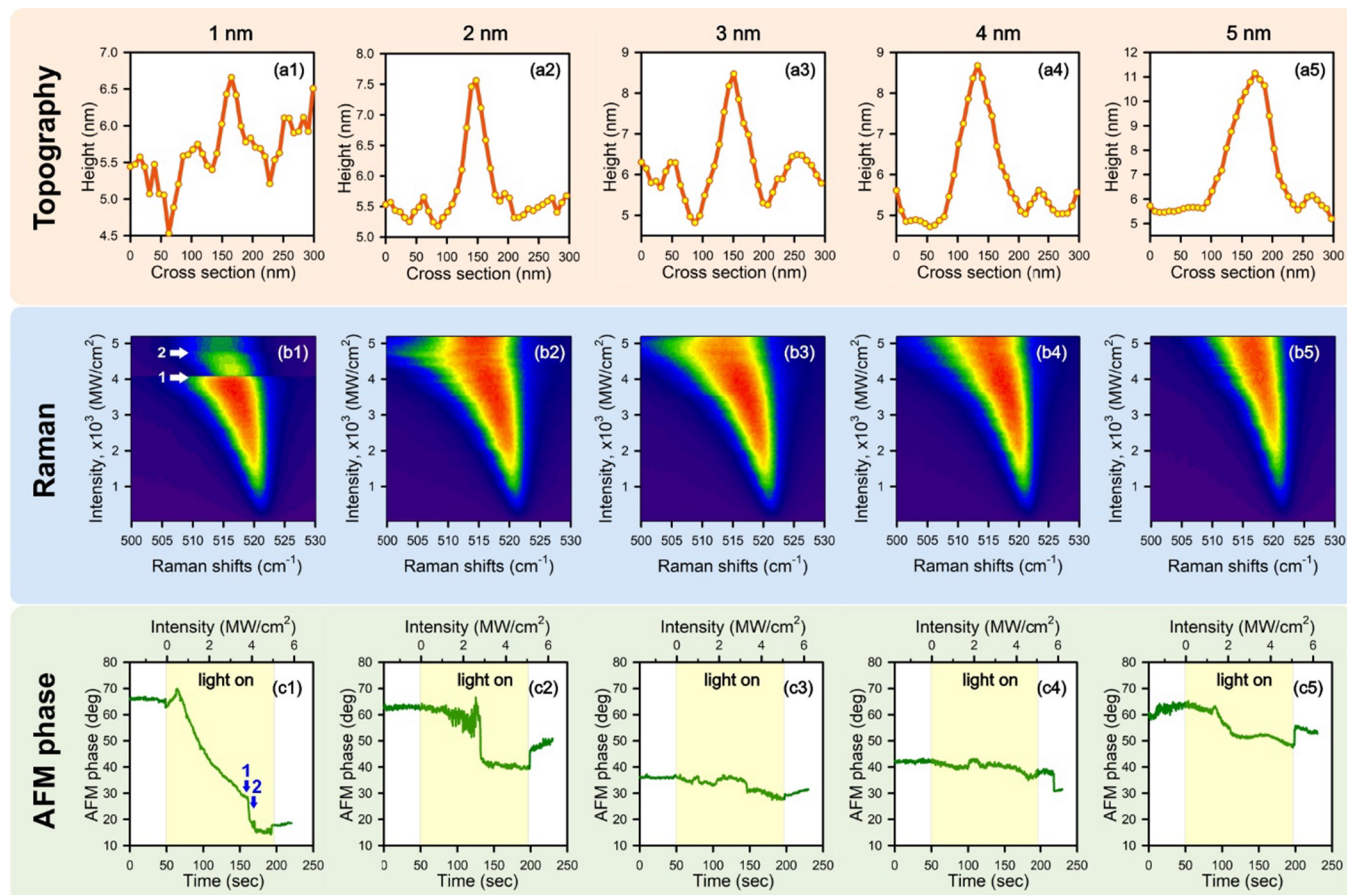
Figure 3. Sensing of tip apex temperature through Raman thermometry and cantilever phase evolution. (a1−a5) AFM topography cross-section of preliminary identified gold structures. (b1−b5) Raman spectrum evolution and (c1−c5) phase dynamic as a functions of input light intensity. The data clearly show that the Si cantilever temperature is inversely proportional to structure size.

temperature increase at the tip apex is $\Delta T \sim 25$ K under the highest illumination doses used in the experiment (Figure SF4e). The simulations also show that the temperature change of the Au substrate is much smaller, as would be expected based on its higher thermal conductivity. We note that the simulated temperature profile of the tip shows a plateau that stretches out to $z = 150$ nm, which becomes especially evident at higher illumination doses (yellow areas, Figure SF4e,f). This geometry-dependent thermal bottleneck is likely due to the decrease of thermal conductivity κ with temperature,[38] and the size-dependent effect.[34] The simulations align closely with the experimental findings (Figure 2g,h), showing tip detachment at $z \sim 165$ nm. It is also clear that to initiate melting, a significant increase (>20 fold) of the maximum optical flux used in the experiment would be necessary, as illustrated in Figure SF4f. Both experimental data and simulations converge on the conclusion that *neither plasmonic effects nor geometry-induced field enhancement can account for the observed optical heating of the Si tip apex* and as such a different mechanism must be at play to explain the results.

To further confirm the increased absorption in Si under photon confinement conditions, we perform measurements when the Si tip is placed over Au structures of a well-defined size. For this purpose, the film is analyzed by AFM imaging to identify individual and isolated Au structures within the 1−5 nm range (Figure 3a1−a5). We record both the temperature dependence of the Raman spectrum (Figure 3b1−b5) and the cantilever phase φ (Figure 3c1−c5), which serves as another

probe that is sensitive to changes in the tip−sample interaction. The phase is especially sensitive to the thermal expansion/contraction of the tip apex or the sample, which is particularly extreme during melting and deformation (see Supporting Information Part 5).

We observe an inverse relationship between particle size and optical heating, as revealed by both Raman (Figure 3b2−b5) and phase measurements (Figure 3c1−c5). For a 1 nm Au structure, the Raman spectra indicate significant optical heating ($\Delta T > 1500$ K), corroborated by the dramatic changes in the cantilever phase, both pointing to the melting of the tip. On the other hand, when the tip is brought into close proximity to structures larger than 3 nm, the temperature change is much smaller ($\Delta T \sim 200$ K for 5 nm) and the tip apex remains fully intact. Note that because of irreversible changes in tip morphology, we used different AFM cantilevers for different experiments. The observed temperature trends are reproducible with every cantilever used and for each gold structure identified. For example, as seen in Figure 3b1−b5, below a laser intensity of 3 MW/cm², the temperature change is fully reversible (see Supporting Information, Part 6, Figure SF5) and the tip apex remains unaffected. These experiments reveal that the optical absorption in Si grows much stronger when the size of the light-trapping nanostructures is decreased from 5 to 1 nm.

As a control experiment, we perform similar measurements with Si AFM cantilevers that are coated with a 30 nm Pt/Ir film. Using the cantilever phase as the readout, we observe a
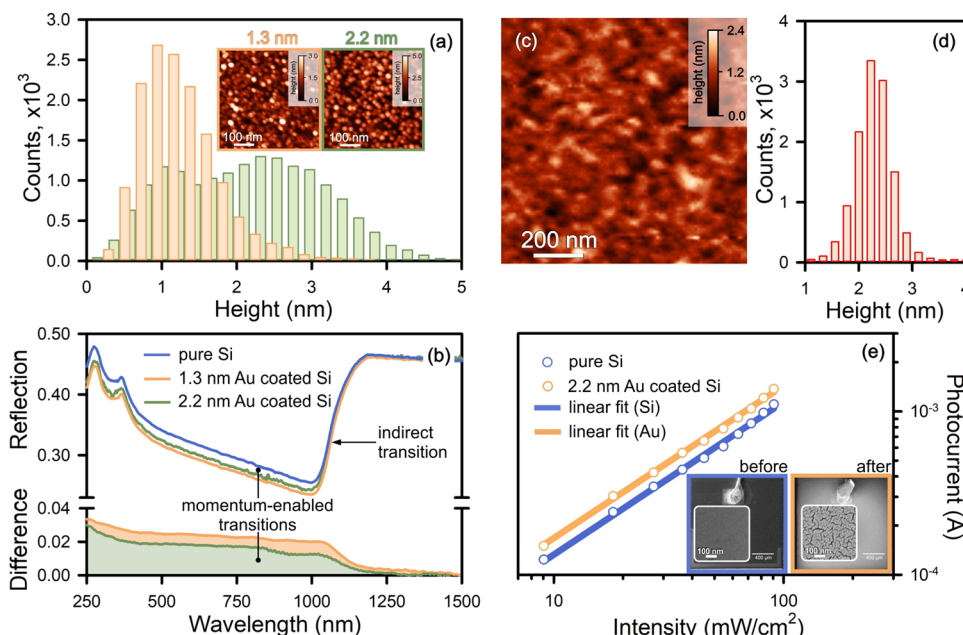
Figure 4. Experiments on Si wafers with deposited Au structures. (a) Height distribution histogram of a single layer of Au nanoparticles of heights ∼1.3 and ∼2.2 nm. (b) Visible/near-infrared reflection spectra of clean and coated Si wafers. Smaller particles provide broader momenta distribution, hence resulting in stronger and spectrally broader absorption enhancement. (c, d) AFM image and height distribution histogram of Au-coated surface Si wafer after sputtering. (e) Photocurrent input power density dependence of Si photodiode with clean (blue) and coated (orange) photosensitive layer. The data show a ∼25% increase in detector responsivity for 2.2 ± 0.5 nm Au structures.

vanishingly small variation upon increasing the laser intensity, indicating insufficient optical heating and no structural damage to the tip or the sample (Figure SF6). This observation underlines that the close proximity of bare Si to a nanometer-size structure is required for enhanced optical absorption in Si.

The anomalous heating of bare Si near the nanometer structure, the efficiency of which is inversely proportional to particle size, cannot be explained through field enhancement in the context of indirect optical transitions in Si. Note that this trend also excludes a prominent role for propagating surface plasmon polaritons at the gold/air surface as their excitation efficiency at asperities is expected to grow with the size of the nanostructure, which is the opposite of the heating trend observed. On the other hand, the highly localized optical fields at the apex of nanostructures in the range $\sigma_r \sim 0.5-2.5$ nm can provide the necessary boost to the momentum of the photon, $p \propto 1/\sigma_r$ to induce direct optical transitions (Figure 1b). This mechanism of increased photon momentum is consistent with the observed inverse dependence of the absorption enhancement on the size of the nanostructure.

The altered absorption rates in silicon near nanometer-sized structures are also predicted by a simple rate analysis. The full effect of absorption enhancement has two contributions, namely, the increase of photon momentum by 2−3 orders of magnitude and the Purcell effect. First, we assume a photon field of the form $E(r, t) = E_0\hat{e}\cdot\mathcal{E}(r)e^{-i\omega t}$,[39] where ω is the angular frequency, $\hat{e}$ is the polarization state, $E_0 = \sqrt{\hbar\omega/(2V_0\varepsilon_0)}$, and $\mathcal{E}(r)$ is the spatial mode function. Fermi's golden rule for a transition from a given Bloch state $|v, k\rangle$ with crystal momentum vector k in the valence band to all possible final states $|c, k'\rangle$ in the conduction band can then be written as

$$W_{vc}(k) = \sum_{k'} \frac{2\pi}{\hbar}\left(\frac{e}{\omega m}\right)^2\left(\frac{\hbar\omega}{2V_0\varepsilon_0}\right)|\langle c, k'|\mathcal{E}(r)\hat{e}\cdot\hat{p}|v, k\rangle$$
$$|^2\delta[\hbar\omega - E_{vc}(k, k')] \tag{1}$$

where $V_0 = q_0^{-3}$ is the mode volume of a photon with wave vector q_0 in free space, $E_{vc}(k, k')$ is the energy difference between band states, and $\hat{p}$ is the momentum operator. In the case of a free space photon, $\mathcal{E}(r) = e^{iq_0 r}$, thus the transition rate is found as

$$W_{vc}(k) \propto \frac{1}{V_0}|\mu_{cv}|^2\delta[\hbar\omega - E_{vc}(k, k + q_0)] \tag{2}$$

where $|\mu_{cv}|^2$ is the transition dipole moment. Since $q_0 \ll k$, only transitions for which $k' \approx k$ are allowed, which translates into vertical transitions. For the confined photon, we choose a spatial mode function $\mathcal{E}(r)$ that resembles a stationary Gaussian distribution with standard deviation σ_r:

$$\mathcal{E}(r) = e^{-r^2/4\sigma_r^2} = \frac{1}{2\pi^2}\int G(q)e^{iqr}d^3q \tag{3}$$

which is written here in terms of a spherically symmetric, three-dimensional Fourier transformation of the momentum distribution function $G(q)$. Although this mode function is a simplification, it, nonetheless, provides an intuitive explanation of the confinement effect on the transition rate. In this scenario, eq 1 yields the transition rate:

$$W_{vc}(k) \propto \frac{1}{V_e}|\mu_{cv}|^2\int d^3q e^{-q^2/4\sigma_q^2}\delta[\hbar\omega - E_{vc}(k, k + q)] \tag{4}$$

where σ_q is the standard deviation of the photon wave vector distribution, and $V_e = \overline{\varepsilon}V$ is the effective mode volume with $\overline{\varepsilon} = \langle\mathcal{E}|\varepsilon|\mathcal{E}\rangle$ the expectation value of the local dielectric (see Supporting Information, Part 2). In a comparison of eqs 2 and

4, it can be seen that this simple model predicts an enhanced absorption rate when the photon is confined to the (sub)-nanometer scale. First, eq 4 shows that transitions between different momentum states of the material are now allowed, weighted by a Gaussian distribution of photon momenta $\hbar q$. The transition further benefits from the integration over all q made available by photon confinement, thus accelerating its rate relative to the free space result in eq 2. Second, the local intensity is enhanced by the mode confinement V_0/V_e, where $V_0 = k_0^{-3}$ is the free space volume of the photon. However, our FDTD simulation shows that the field enhancement due to mode confinement is a relatively small effect, likely caused by a significant increase of $\overline{\varepsilon}$ in the case of the nm-confined photon, thus reducing the V_0/V_e enhancement effect. In short, field enhancement cannot explain the increased absorption on its own (see Supporting Information Part 7), identifying the broadened photon momentum distribution as the prime mechanism for the observed effect.

We expect that the spectral profile of the increased optical absorption due to sub-5 nm photon confinement is not colored by the spectral shape of a plasmon resonance. To examine the predicted spectral response of photon momentum-enabled transitions, we carried out reflectance measurements on Si wafers covered with gold nanoparticles. Deposition of nanoscale structures on Si surfaces and within the crystal bulk has been actively pursued for enhancing the efficiency of solar cells[16,40] and photodetectors.[41] Previous work has aimed at increasing the density of optical states through local field enhancement, using larger (>20 nm) particles and structures. In contrast, here we use Au structures that are significantly smaller, in the 1−2 nm range, where the plasmon resonance is strongly damped through surface scattering.[42] We deposit Au nanoparticles of a particular size distribution to form single-layer films in direct contact with the Si surface (see Supporting Information Part 8). Figure 4a shows AFM images and the height distribution for samples prepared with ∼1.3 and ∼2.2 nm particles. The reflection spectra are obtained with an integrating sphere in diffuse reflection mode (see Methods) and are shown in Figure 4b. The difference in the reflectance spectra between the bare wafer and the covered wafer shows an abrupt reduction of light reflection near the band edge, at 1100 nm, and a lower but otherwise flat response throughout the UV-IR. The reduced reflectance can be explained as direct absorption or, equivalently, as the diagonal optical transitions shown in Figure 1b. Consistent with the mechanism of increased photon momentum, the effect is inversely proportional to the particle size (Figure 4b). This interpretation implies that upon illumination of the decorated surface, photons become trapped at nanometric asperities with finite probability and introduce a noticeable effect on the surface's optical properties. Note that the reflectance spectra are devoid of any spectral signatures of plasmonic resonances, and that silicon's absorption coefficient appears uniformly enhanced along most of the solar spectrum. A rough quantitative estimation of the magnitude of absorption enhancement is provided in Supporting Information Part 10.

Finally, in an arrangement more closely related to photo-detection and photovoltaic applications, using a different sputtering approach (see Methods and Supporting Information Part 11, Figures SF12−SF14), we deposit Au structures on the top surface of the photosensitive layer of a conventional Si photodiode. A representative AFM image of the deposited Au structures, along with their height distribution, is shown in Figure 4c,d. Figure 4e shows the photocurrent detected from the clean (blue) and coated (orange) devices, measured as a function of the incident intensity of a 633 nm laser light source. The data show an increase of detector responsivity from 0.33 to 0.42 A/W, a nearly 25% increase in the amount of generated photoconduction electrons, despite the presence of Rayleigh scattering at larger Au structures and islands. While >50% of the light at 633 nm should be absorbed within the first 2.5 μm of the material,[5] the observed detection enhancement corresponds to an absorption increase by *more than 2 orders* of magnitude since the confined photon absorption takes place within the first ∼2 nm of the top photosensitive layer surface. At the same time, the discussed device demonstrates a straightforward method to enhance detector properties without the need for particle synthesis and deposition. A brief sputtering of metal onto the surface is sufficient to create ∼nm protrusions, significantly expand the momentum distribution, and change the optical properties of silicon at the detector surface's p-layer. In all, similar to the tip heating experiments and the reflectance measurements on a decorated Si surface, the enhancement observed in the photocurrent experiment is in line with the hypothesis of increased absorption due to the widened momentum distribution of the confined photon.

CONCLUSIONS

Efforts to increase light absorption in silicon have hitherto focused primarily on trapping light in a given volume V to increase its path length or field-enhancement mechanisms.[11,16] In the latter case, plasmonic antennas have been leveraged to redistribute the far-field intensity I_0 to a locally confined intensity $I = g^2 I_0$, (g is the field-enhancement factor) in an attempt to increase the absorbed power within a particular volume V to $P \sim \alpha_{\text{indirect}} VI = \alpha_{\text{indirect}} V g^2 I_0$.[11,15,16] In the present work, we achieve absorption enhancement via a different route, namely, by the anomalous optical properties of silicon that are manifested when the indirect semiconductor is put in proximity to structures of <3 nm in size. First, our TERS experiments with Si tips reveal an unusual optical heating effect at the nanoscale. Second, we have observed a similar enhanced optical response in reflection measurements on Si wafers decorated with nm-sized gold structures and in photocurrent measurements with Au-coated Si photodiodes. These phenomena cannot be explained through surface plasmon or geometry-dependent field-enhancement mechanisms, as these are negligible for structures of this size. In addition, the absorption increase is inversely proportional to the size of the structures (Figures 3 and 4), which is opposite to the simulated field-enhancement effects.

Our experiments emphasize that for light confined to nanometric scales its subsequent interaction with matter differs substantially from that enabled by plane waves. Confinement provides a boost of photon momentum by 2 orders of magnitude that opens up optical transitions forbidden for plane waves, effectively changing the material's absorption property. Whereas the light is confined, the semiconducting material is not necessarily altered, thus retaining its electronic structure, as is the case in the experiments on bulk Si presented here. Nanometer confinement of the photon represents an alternative route to increasing the absorbed power $P = \alpha_{\text{direct}} VI$ through the effective change of the absorption coefficient α_{direct} of the medium. This enhancement is not limited to the momentum matching along the Γ to X path in k-space, as

shown for simplicity in Figure 1b. For a given photon energy, a broad momentum distribution enables transitions from multiple points and in any direction across the Brillouin zone as long as available energies and momenta are conserved.

In contrast to the relatively narrow spectral width of plasmonic or geometry-governed resonances, the mechanism of increased photon momentum offers enhancement of the optical absorption from the ultraviolet to the near-infrared, turning indirect semiconductor-like silicon into a direct broadband absorber that resembles a blackbody absorber across three spectral octaves. The experimental results presented here provide an interesting opportunity to reconsider the role of photon momentum in light-matter interactions. With current advances in semiconductor fabrication techniques approaching a resolution of sub-1.5 nm,[43] the effect has the potential to strongly impact not only optical spectroscopies but also photosensing and light-energy conversion technologies.

METHODS

FDTD/FEM Calculation. 3D simulation of optical absorption of a cone-shaped Si tip under cw-focused illumination was performed by using an Ansys/Lumerical FDTD solver. A mesh overlayer of 0.1 nm was utilized around the Au bump and the Si tip apex, and a rougher 1 nm mesh was utilized for the rest of the structure. Perfectly matching layers were used as boundary conditions in three directions. The optical and thermal properties of Si and Au were imported from the Ansys/Lumerical material database. The Si tip apex was exposed to a 632.8 nm focused laser light (NA= 0.7) with the intensity of 5 MW/cm^2. The temperature profile was calculated through an Ansys/Lumerical FEM solver in the steady-state regime. The thermal conductivities of all constituents are assumed to be temperature-independent. The boundary condition of T = 300 K was set at the z_{min} = −3500 nm of the $20 \times 20 \times 5$ μm^3 simulation region.

Atomic Force Microscopy. The multimode scanning probe microscope Prima (NT-MDT) was utilized for visualizing a topography of the intrinsic Si wafer with sputtered Au nanoparticles. AFM cantilever (VIT_P) was made of antimony-doped single-crystal silicon (n-type, 0.01−0.025 Ohm-cm). The tip height is 14−16 μm, the tip curvature radius is 30 nm, and the resonant frequency is 300 kHz.

Scanning Electron Microscopy. The elemental composition and morphology of the samples were studied by the Auriga Crossbeam Workstation (Carl Zeiss AG, Oberkochen, Germany), equipped with an INCA X-Max silicon drift detector (Oxford Instruments, Abingdon, UK) for energy-dispersive X-ray microanalysis. For elemental analysis of Si diodes and wafers, an acceleration voltage of 5 keV, an analytical working distance of 4 mm, and an electron probe current of 75 pA were used (see Supporting Information Part 12 for details).

Light Reflection Measurement. Total reflection spectroscopy on an undoped 280 μm < 100> Si wafer coated with Au nanoparticles was performed using a Jasco V-670 absorption spectrometer equipped with 60 mm integrating sphere. All measurements were performed at 200−2000 nm spectral range with 2 nm spectral resolution.

Specular reflection measurements on Si wafers sputtered with Au were performed using a variable-angle spectroscopic ellipsometer (VASE by J.A. Woollam Co., Inc.) equipped with an Autotrader. The reflection spectra were recorded across a broad spectral range (250 to 2000 nm) with 400 μm beam spot size on the sample at 70° incident angle.

Far- and Near-Field Raman Spectroscopy and Microscopy. Raman spectra and maps were captured with a multipurpose analytical instrument NTEGRA SPECTRA (NT-MDT) in both upright and inverted configurations. The confocal spectrometer was wavelength-calibrated with a crystalline silicon (100) wafer by registering the first-order Raman band at 521 cm^{-1}. A sensitivity of the spectrometer was as high as ca. 2500 photon counts per 0.1 s provided that we used a 100× objective (N.A. = 0.7), an exit slit (pinhole) of 100 μm and a linearly polarized light with the wavelength of 632.8 nm and the power at the sample of 10 mW. No signal amplification regimes of a Newton EMCCD camera (ANDOR) were used.

Magnetron Sputtering. The surface of silicon wafers and diodes was coated with a gold (99.999% purity) nanolayer by using a sputter coater, Quorum Q150R ES Plus (Quorum Tech), for negative glow discharge at an applied current of 20 mA and a sputter vacuum value of 10^{-4} mbar. See Supplementary Information Part 10 for details.

ASSOCIATED CONTENT

Data Availability Statement

S.S.K.; A.I.N.; E.I.B.; L.K.; A.B.K.; J.M.; E.O.P.; V.A.A.; D.A.F.; photon momentum enabled light absorption in bulk silicon. 2023, 2304.14521. arXiv. https://doi.org/10.48550/arXiv.2304.14521 (accessed April 27, 2023).

Ⓢ Supporting Information

The Supporting Information is available free of charge at https://pubs.acs.org/doi/10.1021/acsnano.4c02656.

Nature of the confined photon, Raman thermometry, heat distribution simulations, and an estimation of the absorption enhancement; procedures and methods used for Au sputtering, Au particle preparations and deposition on Si surface, ion milling, and characterization of the Si photodiode; images taken with 3D confocal Raman microscopy in an inverted configuration, heating and cooling of bare and coated Si cantilevers, AFM images and cantilever phase, and a simulation of field enhancement by particles of different sizes (PDF)

AUTHOR INFORMATION

Corresponding Authors

Sergey S. Kharintsev − *Department of Optics and Nanophotonics, Institute of Physics, Kazan Federal University, Kazan 420008, Russia;* ⓘ orcid.org/0000-0002-5788-3401; Email: skharint@gmail.com

Dmitry A. Fishman − *Department of Chemistry, University of California Irvine, Irvine, California 92697, United States;* ⓘ orcid.org/0000-0001-6287-2128; Email: dmitryf@uci.edu

Authors

Aleksey I. Noskov − *Department of Optics and Nanophotonics, Institute of Physics, Kazan Federal University, Kazan 420008, Russia*

Elina I. Battalova − *Department of Optics and Nanophotonics, Institute of Physics, Kazan Federal University, Kazan 420008, Russia*

Liat Katrivas − *George S. Wise Faculty of Life Sciences, Tel Aviv University, Tel Aviv 6997801, Israel*

Alexander B. Kotlyar − *George S. Wise Faculty of Life Sciences, Tel Aviv University, Tel Aviv 6997801, Israel*

Jovany G. Merham − *Department of Chemistry, University of California Irvine, Irvine, California 92697, United States;* ⓘ orcid.org/0000-0003-3151-1877

Eric O. Potma − *Department of Chemistry, University of California Irvine, Irvine, California 92697, United States;* ⓘ orcid.org/0000-0003-3916-6131

Vartkess A. Apkarian − *Department of Chemistry, University of California Irvine, Irvine, California 92697, United States;* ⓘ orcid.org/0000-0002-7648-5230

Complete contact information is available at:
https://pubs.acs.org/10.1021/acsnano.4c02656

Notes

The authors declare no competing financial interest.

REFERENCES

(1) Green, M. A. Self-consistent optical parameters of intrinsic silicon at 300K including temperature coefficients. *Sol. Energy Mater. Sol. Cells* **2008**, *92*, 1305−1310.

(2) Kangsabanik, J.; Svendsen, M. K.; Taghizadeh, A.; Crovetto, A.; Thygesen, K. S. Indirect Band Gap Semiconductors for Thin-Film Photovoltaics: High-Throughput Calculation of Phonon-Assisted Absorption. *J. Am. Chem. Soc.* **2022**, *144*, 19872−19883.

(3) Philipps, S. *Fraunhofer ISE photovoltaics report 2020*; Fraunhofer ISE, 2020.

(4) Chen, H.-L.; et al. A 19.9%-efficient ultrathin solar cell based on a 205-nm-thick GaAs absorber and a silver nanostructured back mirror. *Nature. Energy* **2019**, *4*, 761−767.

(5) Green, M. A.; Keevers, M. J. Optical properties of intrinsic silicon at 300 K. *Progress in Photovoltaics* **1995**, *3*, 189−192.

(6) Turner, W. J.; Reese, W. E.; Pettit, G. D. Exciton Absorption and Emission in InP. *Phys. Rev.* **1964**, *136*, A1467−A1470.

(7) Aspnes, D. E.; Studna, A. A. Dielectric functions and optical parameters of Si, Ge, GaP, GaAs, GaSb, InP, InAs, and InSb from 1.5 to 6.0 eV. *Phys. Rev. B* **1983**, *27*, 985−1009.

(8) Jaffe, J. E.; Zunger, A. Theory of the band-gap anomaly in AB C2 chalcopyrite semiconductors. *Phys. Rev. B* **1984**, *29*, 1882−1906.

(9) Ballif, C.; Haug, F.-J.; Boccard, M.; Verlinden, P. J.; Hahn, G. Status and perspectives of crystalline silicon photovoltaics in research and industry. *Nature Reviews Materials* **2022**, *7*, 597−616.

(10) Louwen, A.; van Sark, W.; Schropp, R.; Faaij, A. A cost roadmap for silicon heterojunction solar cells. *Sol. Energy Mater. Sol. Cells* **2016**, *147*, 295−314.

(11) Saive, R. Light trapping in thin silicon solar cells: A review on fundamentals and technologies. *Progress in Photovoltaics* **2021**, *29*, 1125−1137.

(12) Liu, X.; et al. Black silicon: fabrication methods, properties and solar energy applications. *Energy Environ. Sci.* **2014**, *7*, 3223−3263.

(13) Yablonovitch, E. Statistical ray optics. *J. Opt. Soc. Am.* **1982**, *72*, 899−907.

(14) Wang, K. X.; Yu, Z.; Liu, V.; Cui, Y.; Fan, S. Absorption Enhancement in Ultrathin Crystalline Silicon Solar Cells with Antireflection and Light-Trapping Nanocone Gratings. *Nano Lett.* **2012**, *12*, 1616−1619.

(15) Polman, A.; Atwater, H. A. Photonic design principles for ultrahigh-efficiency photovoltaics. *Nat. Mater.* **2012**, *11*, 174−177.

(16) Atwater, H. A.; Polman, A. Plasmonics for improved photovoltaic devices. *Nat. Mater.* **2010**, *9*, 205−213.

(17) Enrichi, F.; Quandt, A.; Righini, G. C. Plasmonic enhanced solar cells: Summary of possible strategies and recent results. *Renewable and Sustainable Energy Reviews* **2018**, *82*, 2433−2439.

(18) Bharadwaj, P.; Deutsch, B.; Novotny, L. Optical Antennas. *Adv. Opt. Photon.* **2009**, *1*, 438−483.

(19) Novotny, L.; Hecht, B. *Principles of Nano-Optics*, 2nd ed.; Cambridge University Press, 2012.

(20) Zhang, P.; Feist, J.; Rubio, A.; García-González, P.; García-Vidal, F. J. Ab initio nanoplasmonics: The impact of atomic structure. *Phys. Rev. B* **2014**, *90*, No. 161407.

(21) des Francs, G. C.; et al. Plasmonic Purcell factor and coupling efficiency to surface plasmons. Implications for addressing and controlling optical nanosources. *J. Opt.* **2016**, *18*, No. 094005.

(22) Urbieta, M.; et al. Atomic-Scale Lightning Rod Effect in Plasmonic Picocavities: A Classical View to a Quantum Effect. *ACS Nano* **2018**, *12*, 585−595.

(23) Baumberg, J. J. Picocavities: a Primer. *Nano Letters* **2022**, *22*, 5859−5865.

(24) Höppener, C.; et al. Tip-enhanced Raman scattering. *Nature Reviews Methods Primers* **2024**, *4*, 47.

(25) Lee, J.; Crampton, K. T.; Tallarida, N.; Apkarian, V. A. Visualizing vibrational normal modes of a single molecule with atomically confined light. *Nature* **2019**, *568*, 78−82.

(26) Zhang, Y.; et al. Visually constructing the chemical structure of a single molecule by scanning Raman picoscopy. *National Science Review* **2019**, *6*, 1169−1175. %J National Science Review (

(27) Shalaev, V. M.; Douketis, C.; Haslett, T.; Stuckless, T.; Moskovits, M. Two-photon electron emission from smooth and rough metal films in the threshold region. *Phys. Rev. B* **1996**, *53*, 11193−11206.

(28) Kurman, Y.; et al. Control of semiconductor emitter frequency by increasing polariton momenta. *Nat. Photonics* **2018**, *12*, 423−429.

(29) Trolle, M. L.; Pedersen, T. G. Indirect optical absorption in silicon via thin-film surface plasmon. *J. Appl. Phys.* **2012**, *112*, No. 043103.

(30) Noda, M.; Iida, K.; Yamaguchi, M.; Yatsui, T.; Nobusada, K. Direct Wave-Vector Excitation in an Indirect-Band-Gap Semiconductor of Silicon with an Optical Near-field. *Physical Review Applied* **2019**, *11*, No. 044053.

(31) Yamaguchi, M.; Nobusada, K. Indirect interband transition induced by optical near fields with large wave numbers. *Phys. Rev. B* **2016**, *93*, No. 195111.

(32) Yatsui, T.; et al. Enhanced photo-sensitivity in a Si photodetector using a near-field assisted excitation. *Communications Physics* **2019**, *2*, 62.

(33) Macfarlane, G. G.; Roberts, V. Infrared Absorption of Silicon Near the Lattice Edge. *Phys. Rev.* **1955**, *98*, 1865−1866.

(34) Kharintsev, S. S.; et al. Designing two-dimensional temperature profiles using tunable thermoplasmonics. *Nanoscale* **2022**, *14*, 12117−12128.

(35) Kharintsev, S. S.; et al. Light-Controlled Multiphase Structuring of Perovskite Crystal Enabled by Thermoplasmonic Metasurface. *ACS Nano* **2023**, *17*, 9235.

(36) Odom, T. W.; Schatz, G. C. Introduction to Plasmonics. *Chem. Rev.* **2011**, *111*, 3667−3668.

(37) Baffou, G.; Cichos, F.; Quidant, R. Applications and challenges of thermoplasmonics. *Nat. Mater.* **2020**, *19*, 946−958.

(38) Shanks, H. R.; Maycock, P. D.; Sidles, P. H.; Danielson, G. C. Thermal Conductivity of Silicon from 300 to 1400 K. *Phys. Rev.* **1963**, *130*, 1743−1748.

(39) Loudon, R. *The Quantum Theory of Light*; OUP Oxford, 2000.

(40) Pillai, S.; Catchpole, K. R.; Trupke, T.; Green, M. A. Surface plasmon enhanced silicon solar cells. *J. Appl. Phys.* **2007**, *101*, No. 093105.

(41) Stuart, H. R.; Hall, D. G. Island size effects in nanoparticle-enhanced photodetectors. *Appl. Phys. Lett.* **1998**, *73*, 3815−3817. %J Applied Physics Letters (

(42) Hartland, G. V.; Besteiro, L. V.; Johns, P.; Govorov, A. O. What's so Hot about Electrons in Metal Nanoparticles? *ACS Energy Letters* **2017**, *2*, 1641−1653.

(43) Tseng, L.-T.; et al. Resistless EUV lithography: Photon-induced oxide patterning on silicon. *Science Advances* **2023**, *9*, No. eadf5997.